atmosphere

MDPI

Article

Near-Surface Thermodynamic Influences on Evaporation Duct Shape

Sarah E. Wessinger [1,2], Daniel P. Greenway [1], Tracy Haack [2,†] and Erin E. Hackett [1,*]

[1] Department of Marine Science, Coastal Carolina University, Conway, SC 29528, USA; sewessing@coastal.edu (S.E.W.); dpgreenwa@coastal.edu (D.P.G.)
[2] Marine Meteorology Division, Naval Research Laboratory, Monterey, CA 93943, USA
* Correspondence: ehackett@coastal.edu
† Retired.

Abstract: This study utilizes *in situ* measurements and numerical weather prediction forecasts curated during the Coupled Air–Sea Processes Electromagnetic Ducting Research (CASPER) east field campaign to assess how thermodynamic properties in the marine atmospheric surface layer influence evaporation duct shape independent of duct height. More specifically, we investigate evaporation duct shape through a duct shape parameter, a parameter known to affect the propagation of X-band radar signals and is directly related to the curvature of the duct. Relationships between this duct shape parameter and air sea temperature difference (ASTD) reveal that during unstable periods (ASTD < 0), the duct shape parameter is generally larger than in near-neutral or stable atmospheric conditions, indicating tighter curvature of the *M*-profile. Furthermore, for any specific duct height, a strong linear relationship between the near-surface-specific humidity gradient and the duct shape parameter is found, suggesting that it is primarily driven by near-surface humidity gradients. The results demonstrate that an *a priori* estimate of duct shape, for a given duct height, is possible if the near-surface humidity gradient is known.

Keywords: evaporation ducts; evaporation duct shape; log-linear refractivity models; refractivity parameterization; refractivity; specific humidity; atmospheric stability; wind shear

check for updates

Citation: Wessinger, S.E.; Greenway, D.P.; Haack, T.; Hackett, E.E. Near-Surface Thermodynamic Influences on Evaporation Duct Shape. *Atmosphere* **2024**, *15*, 718. https://doi.org/10.3390/atmos15060718

Academic Editors: Yubin Li and Jie Tang

Received: 23 April 2024
Revised: 4 June 2024
Accepted: 11 June 2024
Published: 15 June 2024

Copyright: © 2024 by the authors. Licensee MDPI, Basel, Switzerland. This article is an open access article distributed under the terms and conditions of the Creative Commons Attribution (CC BY) license (https://creativecommons.org/licenses/by/4.0/).

1. Introduction

Varying thermodynamic properties in the marine atmospheric surface layer (MASL) influence variations in the index of refraction. These changes in the index of refraction lead to changes in the direction of electromagnetic (EM) wave propagation, potentially causing the EM signal to bend back towards Earth's surface, resulting in anomalous propagation. In extreme cases of downward refraction, EM signals can be trapped close to the Earth's surface. This phenomenon is known as surface ducting, which notoriously causes target positioning errors, signal loss above the duct, and expanded signal range within the duct for X-band radar. The most common type of surface duct in marine environments is the evaporation duct (ED), which is caused by rapid decreases in humidity with altitude and is a common worldwide feature over marine surfaces [1,2]. Thus, accurately describing EDs is crucial for radar systems operating in marine environments.

Modified refractivity is commonly used in lieu of the index of refraction because it accounts for the curvature of the earth to allow for the easy identification of EDs and amplifies differences in the refractive index from unity. Frequently, especially in radar wave propagation simulations, EDs are modeled using parametric log-linear models, which model vertical distributions of modified refractivity with a limited number of parameters [3–5].

Although more sophisticated methods of predicting refractivity vertical profiles exist, such as using numerical weather prediction (NWP) [6] and Monin–Obukov similarity theory (MOST) [7], some reliance on these simple log-linear models remains for several reasons. One, the required supporting meteorological measurements for implementing

MOST may be lacking. Two, MOST and NWP require a level of expertise to implement that may not be accessible to all scientists and engineers interested in predicting propagation in ducting environments. Finally, in many cases, a simple duct model is more convenient and practical to implement in propagation simulations.

One such example of a parametric modified refractivity model is a two-layer model proposed by Penton and Hackett [8], which is an extension of the classic Paulus–Jeske-type ED model [9,10]. The Penton and Hackett [8] model defines an ED using four parameters: evaporation duct height (z_d), the potential refractivity gradient or duct shape parameter (c_0), mixed layer slope (m_1), and surface modified refractivity (M_0), as depicted in Figure 1,

$$M(z) = M_0 + \left\{ \begin{array}{ll} c_0\left(z - z_d ln\left(\frac{z+z_0}{z_0}\right)\right), & z \le z_L \\ m_1 z - M_1, & z > z_L \end{array} \right\} \quad (1)$$

where z is altitude, M_1 is a parameter that ensures continuity between the two layers (and is defined by the other parameters), z_L is the altitude of the top of the evaporation layer ($z_L \equiv 2z_d$), and z_0 is the aerodynamic roughness factor, which is commonly assumed to be 0.00015 m because it is close to the average value for oceanic conditions [11].

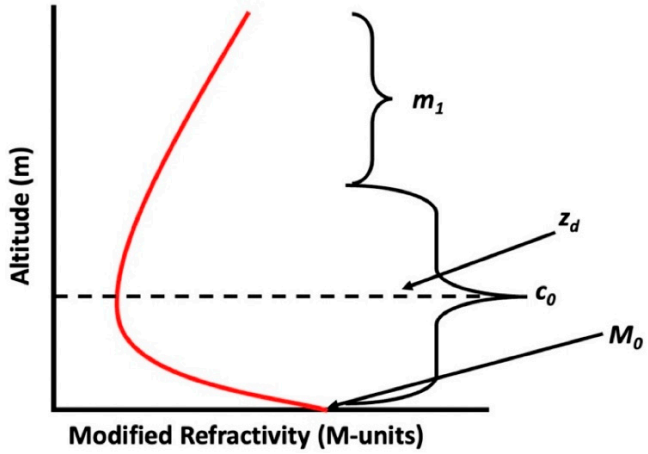


Figure 1. Example of a modified refractivity profile for the two-layer model described by Equation (1) [8] and associated parameters.

Most of the literature [1,12–15] investigating ED M-profiles using similar parametric refractivity models assume c_0 = 0.125 M-units m^{-1}, derived as the critical potential refractivity gradient required for trapping [9]. This value was derived assuming neutral atmospheric stability, a thermodynamic regime that is rarely observed precisely. Multiple recent studies have demonstrated that varying c_0 from the commonly assumed neutral value (i.e., 0.125 M-units m^{-1}) significantly alters EM wave propagation [16,17]. Recent research has also shown that duct height, which also impacts duct shape, can be reasonably estimated (and remotely sensed) from radar measurements using inverse methods [18–20]. The duct height occurs at the altitude where the sign of the vertical gradient of the modified refractivity profile changes sign (or is zero), and it sets the top of the trapping layer. The duct height itself can change the shape of the vertical profile, but for a given duct height, generally speaking, the shape of the duct impacts the duct strength through its modification of the M-deficit (difference between M at the surface and at the duct height) [16].

Presently, little is understood about the connections between the physical environment and the shape of the duct, independent of duct height, and consequently it is not possible to make predictions of this shape parameter (c_0) *a priori*. In other words, although it is known that c_0 should be adjusted from the neutral value, it is unclear how to modify it to account for atmospheric conditions (in a general sense).

Although duct height, z_d (i.e., altitude where $\frac{\partial M}{\partial z} = 0$), and its effects on X-band propagation during evaporative ducting conditions have been studied extensively [2,16,21–23], the

duct shape, independent of duct height, has been studied sparsely. Lentini and Hackett [17] demonstrated that c_0 is more important than z_d at frequencies above X-band at long ranges from the transmitter. Saeger et al. [10] suggested that the decoupling of m_1 and c_0 within a two-layer parametric refractivity model would improve the estimation of *M*-profiles relative to *in situ* (radiosonde) data due to being able to adjust the curvature of the duct independent of duct height, and without altering the mixed layer slope. Pastore at al. [16] also noted that *M*-profile shape, or profile curvature, affects X-band EM wave propagation at long ranges from the transmitter and demonstrated a direct linear relationship between the duct curvature and *M*-deficit, which describes the strength of the duct [12,24]. Here, we focus our investigation on duct shape and duct strength through the lens of this duct shape parameter (c_0).

Few prior studies have examined factors influencing duct shape and related them to atmospheric conditions. Cherrett [24] evaluated atmospheric property relationships with z_d and ED strength (characterized by the *M*-deficit) and found that, in very unstable regimes, both z_d and ED strength are most sensitive to humidity, but in near-neutral cases, there is some dependence on atmospheric stability. Pastore et al. [16] also suggest that ED curvature is likely driven by near-surface gradients of temperature and humidity. Furthermore, Zhang et al., 2017 [25] connected the ED to the physical environment with a log-linear relationship between z_d and evaporation rate. Generally, higher evaporation rates and higher sea surface temperatures (SSTs) often lead to the formation of evaporation ducts under unstable atmospheric conditions, although it is possible for evaporation ducts to form under stable atmospheric conditions as well. Unstable atmospheric conditions also play important roles in forcing mesoscale meteorological events such as mesoscale convective systems and aggravated coastal precipitation events due to sea breezes.

This study examines evaporation duct shape using environmental parameters estimated by NWP and semi-empirical models to identify relationships between the near-surface-specific humidity gradient (NSSHG), the air–sea temperature difference (ASTD), gradient Richardson number (Ri), wind shear, and c_0. Such insights can make *a priori* estimates of c_0, or duct shape, more tractable for implementation in propagation models; this would enable a simple parametric refractivity model to account for variations in duct shape for a given duct height. For example, *a priori* duct shape estimates could help improve propagation predictions without the use of more complex and computationally demanding mesoscale weather models.

2. Data and Analysis Methods

In this section, the datasets used for this study are described, which consist of refractivity predictions from the CASPER east field campaign [26]. Although these are predictions, they have been verified against measured data during this field campaign; thus, they are considered to be of a high quality. Two different numerical datasets are used to reduce the potential of model bias in the results. Although both sets of data rely to some extent on MOST, the differing implementation should help reduce potential for bias. Furthermore, one dataset incorporates measurements made during the campaign, while the other does not (aside from any routine data assimilation). Obtaining consistent results across the two datasets increases confidence in the results. These numerical data are fit to the parametric refractivity model (Equation (1)) to parameterize the duct shape with the duct shape parameter. The details of this fitting to the parametric model are also contained in this section. Finally, this section also describes the meteorological parameters that are evaluated for their relationship with this duct shape parameter and specifies how they are computed from the datasets.

2.1. Numerical Data

The data used in this study come from two subsets of numerical data modeled for conditions during the CASPER east field campaign [26], which is an experimental effort to better understand radar wave propagation during evaporative ducting conditions in the MASL. CASPER-East took place offshore Duck, North Carolina, between 12 October and

6 November 2015. This location and time of year is a prime environment for developing EDs because of the warmer SSTs and cooler air temperatures occurring during the autumn season, especially further offshore, due to the higher SSTs of the Gulf Stream. Warmer SSTs and cooler air temperatures lead to unstable atmospheric conditions promoting steep near-surface humidity gradients. The prominence of the unstable atmospheric condition during the field campaign can be seen in Figure 2 by the negative air–sea temperature differences (ASTDs).

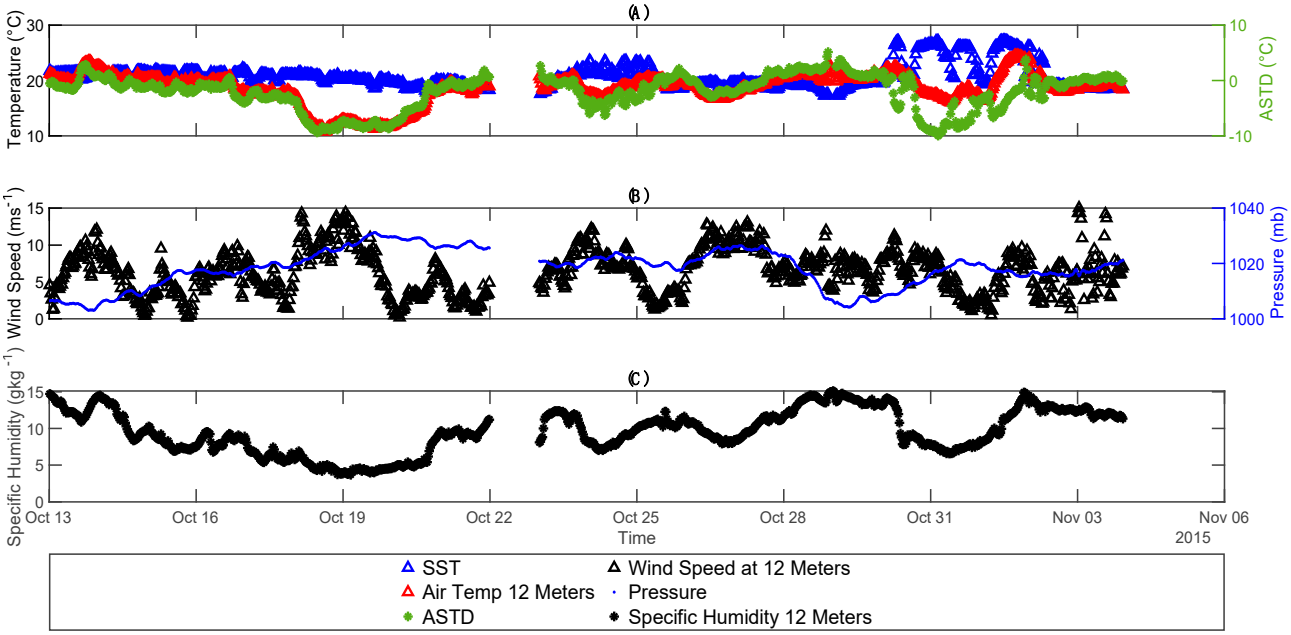


Figure 2. *In situ* bulk measurements from the R/V Sharp used by the COARE algorithm to compute vertical profiles of temperature, wind speed, and specific humidity: (**A**) *in situ* bulk temperature measurements: skin-corrected sea surface temperature (SST) and air temperature 12 m above the sea surface measured from the bow mast of the R/V Sharp. The ASTD (right axis) between these two measurements is used as a rough estimate for observed stability regime. (**B**) *In situ* bulk measurements of wind speed and atmospheric pressure (right axis) at 12 m above the sea surface measured on the bow mast of the R/V Sharp. (**C**) *In situ* bulk measurements of specific humidity 12 m above the sea surface measured on the R/V Sharp bow mast (note the measurement gap in October is due to a mid-cruise port call).

One numerical dataset uses time-averaged (bulk) meteorological measurements and SST measurements taken aboard the research vessel (R/V) Sharp, along with wave spectra from wave buoys, to generate atmospheric profiles of wind speed, temperature, and humidity using the Coupled Ocean Atmosphere Response Experiment (COARE) algorithm that implements MOST [7,27]. Bulk meteorological measurements are 30 min averaged measurements of air temperature, pressure, humidity, and wind speed (see Figure 2) taken approximately 12 m above the sea surface from a bow mast on the R/V Sharp that acquired data at 20 Hz. SST measurements are from the R/V Sharp water intake (~0.1 Hz) and averaged over 5 min intervals and then corrected to skin temperatures using an infrared SST autonomous radiometer (ISAR) skin temperature probe [26]. The surface values are zero for wind, the skin SST for temperature, and surface-specific humidity is approximated from a 98% relative humidity assumption for the given SST.

Wave spectra are computed every 30 min, each from surface displacement time series measured at a sampling frequency of 2 Hz over ~40 s intervals at five fixed buoy locations along an offshore transect between Duck pier and 60 km offshore [16,26]. The power spectral densities (PSDs) of the surface displacements for all 5 buoys for each measurement interval (40 s) are spatially averaged to estimate a mean PSD (1D wave spectrum) for

the region. The 30 min wave spectra can be linked with each R/V Sharp bow mast bulk measurement of the atmospheric properties [16].

COARE determines aerodynamic roughness by incorporating inputs regarding the significant wave height (h_s) and peak wavenumber, which were calculated from the mean PSD:

$$h_s = 4\sqrt{w} \tag{2}$$

where w is the integral of the buoy-averaged 1D wave spectrum. Peak wavenumber is the wavenumber associated with the peak frequency [28], which is the frequency of the highest mean PSD.

COARE atmospheric profiles of temperature, humidity, and pressure are used to calculate vertical profiles, with 0.1 m vertical discretization, of modified refractivity using [29]:

$$N = 77.6\frac{P}{T} + 373256\frac{e}{T^2} \tag{3}$$

where P is pressure (mb), T is temperature (K), and e is partial vapor pressure (mb). Atmospheric refractivity is then converted to modified refractivity:

$$M(z) = \left(n + \frac{z}{R_e} - 1\right) \times 10^6 = N + \frac{z}{R_e} \times 10^6 \tag{4}$$

where R_e is the radius of the earth, and n is the index of refraction. The data comprise 995 COARE M-profiles used in this study.

The second numerical dataset used in this study is curated from the Coupled Ocean-Atmosphere Mesoscale Prediction System (COAMPS® [30]). It consists of NWP forecasts of modified refractivity profiles during CASPER-east, which are blended with the Navy Atmospheric Vertical Surface Layer Model (NAVSLaM; [31]). The initial boundary conditions used in COAMPS® for the atmosphere and ocean are estimated from the Naval Global Environmental Model (NAVGEM [32]) and the Global Hybrid Coordinate Ocean Model (HYCOM [33]), respectively. COAMPS® has a resolution of seventy-one levels between 4 m and 4000 m, of which only six levels are within the lowest 100 m. This resolution is inadequate for EDs. As such, the COAMPS® predictions are blended with NAVSLaM by seeding the NAVSLaM algorithm with COAMPS® estimates to ensure adequate resolution for EDs. NAVSLaM, like COARE, employs MOST to estimate near-surface atmospheric property vertical profiles. Blended profiles generate meteorological estimates for specific humidity, temperature, and wind speed with decimeter vertical sampling within the first 100 m of altitude; the bulk SST from COAMPS® is also used. COAMPS® predictions are initialized every 12 h and consist of hourly forecasts over the duration of the CASPER-east experiment (648 forecasts). Each blended forecast is for 31 offshore locations with a spatial sampling of ~2 km over a 60 km transect beginning at Duck Pier, NC (for a total of 20,088 profiles over all forecasts). An example COAMPS®-NAVSLaM blended forecast is shown in Figure 3. For brevity, COAMPS® will be used subsequently in this manuscript to describe these blended forecasts.

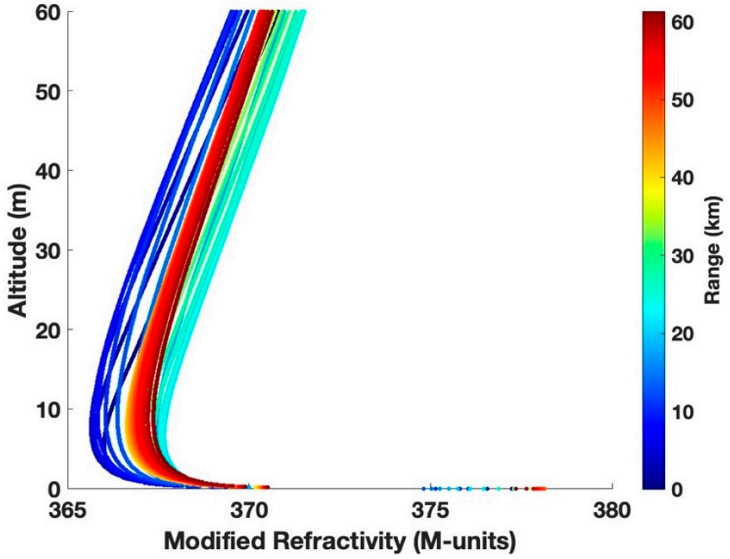


Figure 3. Modified refractivity profiles from a COAMPS® forecast corresponding to October 10th 0600Z; color denotes their respective ranges from Duck pier (see color bar).

2.2. Analysis Methods

The parameters of the parametric model (Equation (1)) [8,34] are estimated from each COARE and COAMPS® modified refractivity profile that contains only an evaporation duct (i.e., elevated and surface-based ducts are not considered). Parameters are estimated either directly from refractivity profiles or through the use of nonlinear-least-squares regression (NLSR). z_d is determined directly as the altitude where the gradient of modified refractivity $\left(\frac{\partial M}{\partial z}\right)$ changes sign. M_0 is directly determined as the modified refractivity at $z = 0$ m. Because c_0 and m_1 must transition as smoothly as possible at the top of the evaporation layer and c_0 is difficult to estimate directly from the data, an NLSR is used to fit the numerical data M-profiles to Equation (1) to estimate c_0 and m_1. The initial guess (for the NLSR) for c_0 is set to the commonly assumed value for neutral stability (0.125 M-units m^{-1}) [9], and the initial guess for m_1 is set to the global average mixed layer slope (0.118 M-units m^{-1}) [35].

To verify the use of c_0 as a proxy for M-profile shape, the average second order derivative $(\overline{\frac{\partial^2 M}{\partial z^2}})$ of the COAMPS® M-profiles is calculated within the evaporation layer (i.e., $z = 0$ to $z = 2z_d$) and evaluated against the NLSR fits of c_0. The average second order derivative has been previously used to characterize duct shape [16], and the comparison of this second order derivative with c_0 enables duct shape to be examined in the context of a parametric refractivity model that can be directly used in propagation simulations. The vertical derivative of M is computed as a central difference aside from the edge points where forward and backward differences are used.

Figure 4A compares an M-profile based on Equation (1), using parameters estimated as described in the preceding paragraph, to the corresponding COAMPS® M-profile. The goodness of the NLSR fit is evaluated via the mean squared error (E_r) within the evaporation layer (i.e., $z = 0$ to $z = 2z_d$) to focus on the duct curvature portion of the refractivity profile. Specifically, E_r is computed as follows:

$$E_r = \frac{1}{n_{mref}} \sum_{i=1}^{n_{mref}} \left(M_{c_i} - \hat{M}_{f_i} \right)^2 \tag{5}$$

where M_c is the COARE or COAMPS® refractivity, $\hat{M}_f$ is the parametric model fit to the COARE or COAMPS® refractivity, and n_{mref} is the number of altitudes within the evaporation layer.

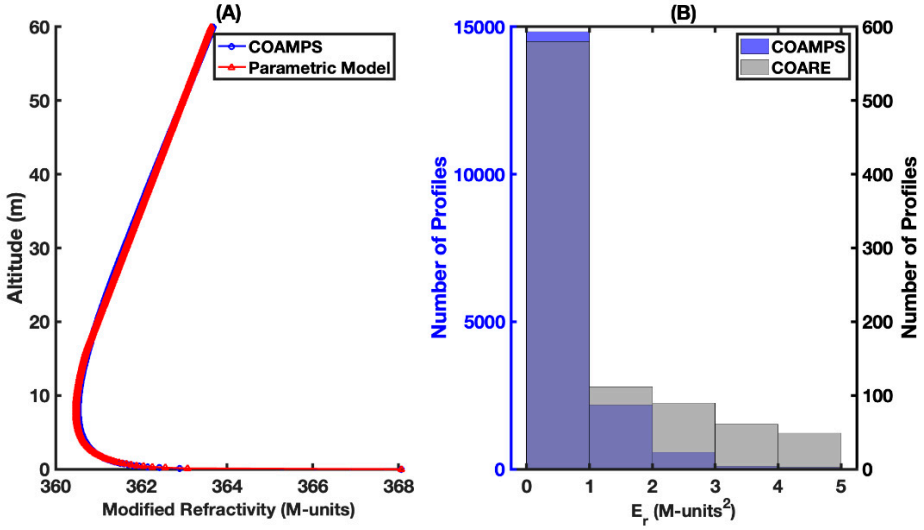


Figure 4. (**A**) Example nonlinear-least-squares regression (NLSR) fit of Equation (1) to a COAMPS® modified refractivity profile. The forecast in this example is for November 3rd 0700Z, which was initialized at 0000 UTC. (**B**) Histograms of E_r for COAMPS® (blue; left axis) and COARE (grey; right axis) (see legend), where bin-overlap is in the alternate shade of blue.

Figure 4B shows the E_r distribution for all CASPER-East numerical data containing EDs, where COAMPS is shown in blue and COARE is shown in gray (note that overlap shows as an alternate shade of blue). Only profiles that fit the parametric model very well ($E_r < 1$ M-unit^2; first bin in Figure 4B) are utilized in this study to evaluate relationships between c_0, atmospheric stability, and NSSHG. This restriction ensures that the results are not influenced by cases where the parametric model fails to properly represent the evaporation duct. We apply this criterion and ~58% of COARE *M*-profiles and ~73% of COAMPS® *M*-profiles are left for use in this study. Recall that the COAMPS® dataset used within this study is approximately 20 times larger than the COARE dataset. In general, the parametric model represents the COAMPS® data better than the COARE data.

c_0 estimated from all the *M*-profiles is analyzed with respect to the co-located and synchronous estimates of the other atmospheric variables. The atmospheric stability's relationship to c_0, and thus ED shape, is explored through two stability metrics: the gradient Richardson number (*Ri*; Equation (6)) and ASTD. *Ri* is a non-dimensional number that represents the ratio between buoyancy-induced turbulence production and shear-induced turbulence production. *Ri* is often considered to be not only an indicator/descriptor of turbulence but is also approximately the same as atmospheric stability when atmospheric conditions are unstable [36,37]. Furthermore, *Ri* encapsulates many physical parameters (temperature, wind components, and humidity); thus, the results of relationships between c_0 and *Ri* may certainly shed light on relationships with other physical parameters. The relationship between *Ri* and c_0 is compared to the relationship between the ASTD and c_0 to evaluate if c_0 behaves similarly with respect to these two stability metrics. The profiles of *Ri* are calculated [36–38]:

$$Ri(z) = \frac{\frac{g}{T_v}\frac{\partial \theta_v(z)}{\partial z}}{\left(\frac{\partial u(z)}{\partial z}\right)^2 + \left(\frac{\partial v(z)}{\partial z}\right)^2} \quad (6)$$

where g is gravitational acceleration (9.81 ms^{-2}), θ_v is virtual potential temperature, T_v is average virtual temperature over all altitudes between the surface, and $z = 2z_d$ and u and v are the east/west and north/south wind components, respectively. *Ri* is calculated at each altitude, and the average *Ri* in the evaporation layer is used to characterize the stability. Note that *Ri* is not examined for COARE as wind direction is not estimated by COARE; thus, COARE does not provide all the required variables for calculating *Ri*

using Equation (6). The ASTD is calculated by subtracting SST from the air temperature predictions at z_L ($z_L = 2z_d$).

NSSHG ($\partial q/\partial z$) and wind speed shear ($\partial U/\partial z$) are also investigated for relationships with c_0. These metrics are calculated by finding the difference between specific humidity or wind speed at $z_L = 2z_d$ and at the surface ($z = 0$ m) and dividing by the difference in altitude, $2z_d$ (i.e., the evaporation layer thickness). These altitudes are chosen to envelop variations spanning the evaporation layer; additionally, it is likely that the constant flux layer begins before $z = 2z_d$, and mathematically, in the two-layered model, c_0 influences the evaporation duct curvature from the surface to $2z_d$. Recall that the surface-specific humidity is estimated using SST for determining vapor saturation values and assuming 98% relative humidity.

Relationships of c_0 with respect to *Ri*, ASTD, wind shear, and NSSHG are evaluated using scatter plots, Pearson's correlation coefficients, and coefficients of determination on regression fits to ascertain connections between c_0 and these physical properties.

3. Results and Discussion

First, we discuss c_0 as a proxy for ED shape. Here, shape is a general term used to describe the vertical trends of refractivity. One way we can quantify the shape is by estimating the mathematical curvature of the vertical *M*-profile (function), which is defined by its second derivative. This quantification of the shape is most logical for an ED because its vertical trend is mostly dictated by the curve of the profile within the duct (i.e., surrounding and below the duct height).

The first derivative of *M* with respect to *z* from Equation (1) within the evaporation layer ($z < z_L$) yields the following:

$$\frac{\partial M}{\partial z} = c_0 + c_0 z_d \left(\frac{1}{z + z_0} \right) \tag{7}$$

and the second derivative is thus

$$\frac{\partial^2 M}{\partial z^2} = \frac{-c_0 z_d}{(z + z_0)^2} \tag{8}$$

Equation (8) shows that the curvature of the *M*-profile is a function of both duct height (z_d) and c_0; thus, the shape of the duct is controlled both by the duct height and this shape parameter (c_0). Varying c_0, therefore, enables a way for the shape of the duct to be altered independent of duct height. Figure 5A illustrates this point by showing two *M*-profiles, both from COAMPS® with $z_d = 13$ m, but different c_0. The profile with the larger c_0 ($c_0 = 0.41$ M-units m^{-1}), denoted in blue, has larger near-surface gradients than the profile with a smaller c_0 ($c_0 = 0.26$ M-units m^{-1}) denoted in red. Thus, although the duct heights (as well as mixed layer slopes) are the same, the ED shape changes with the modification of c_0. Figure 5B further evaluates this shape effect by illustrating the relationship between c_0 and the evaporation layer-averaged second order vertical derivative of modified refractivity ($\overline{\frac{\partial^2 M}{\partial z^2}}$), previously used to describe ED shape in a propagation study [16]. These results illustrate a z_d-dependent linear trend between c_0 and this mathematical quantification of curvature. These results demonstrate that ED shape is related to the c_0 parameter. While the duct height also impacts the shape of the duct, the effects of duct height on propagation as well as its relationship to atmospheric conditions have been extensively studied. Here, we focus on the c_0 parameter as a way of examining the influence of the environment on duct shape independent of the duct height. In fact, and as Equation (8) shows, more than one duct shape can occur for a given duct height, yielding the relationship between the duct curvature ($\overline{\frac{\partial^2 M}{\partial z^2}}$) and c_0, shown in Figure 5B. In contrast, it can also be seen in Figure 5B that there is significant scatter in the relationship between $\overline{\frac{\partial^2 M}{\partial z^2}}$ and c_0, which is due to the duct height also playing a role in determining $\overline{\frac{\partial^2 M}{\partial z^2}}$ (see color bar in Figure 5B; Equation (8)).

Examining the relationship between c_0 and various environmental parameters sheds light on what aspects of the environment might alter duct shape without impacting duct height.

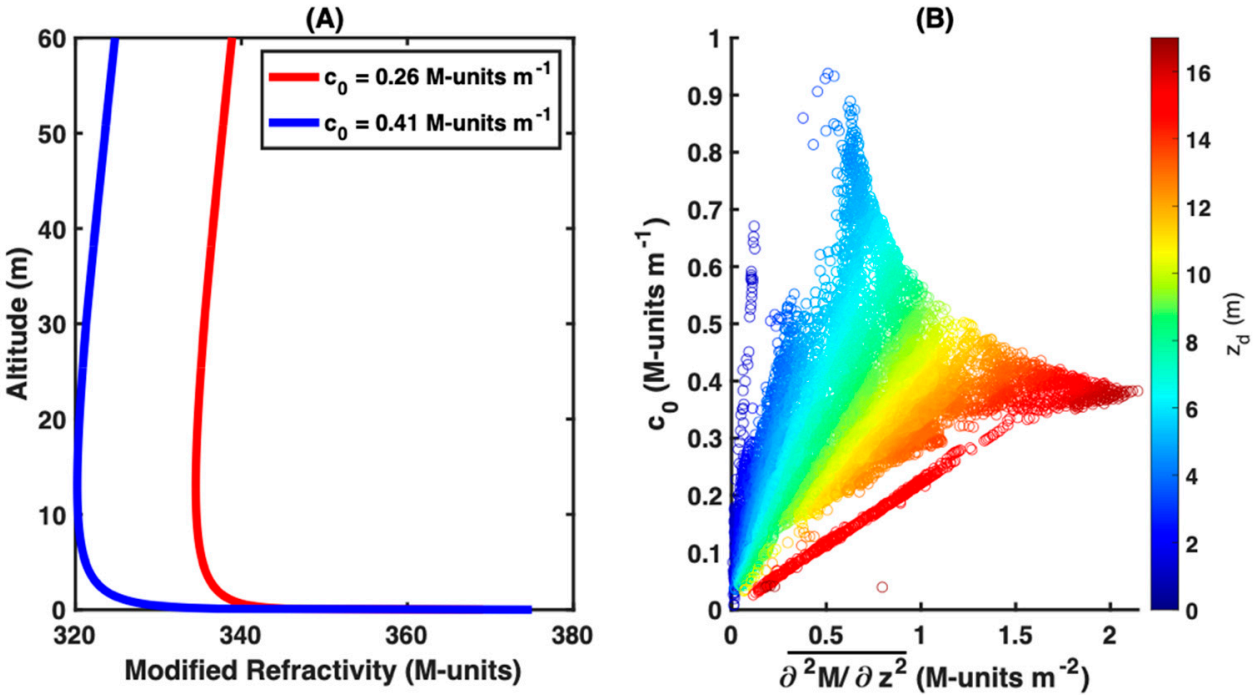


Figure 5. (**A**) NLSR-fits of the parametric refractivity model (Equation (1)) to two COAMPS® *M*-profiles both with z_d = 13 m and m_1 = 0.1 M-units m^{-1}, different c_0 (see legend), and M_0 of 369 and 375 M-units for the red and blue profiles, respectively. (**B**) Scatter plot of NLSR-based c_0 of COAMPS® *M*-profiles and the corresponding evaporation layer-averaged second order vertical derivative of modified refractivity. The colors denote duct height (see color bar).

Because EDs are a common occurrence over marine surfaces in unstable thermal regimes, and rarer in stable thermal regimes due to presumably weaker near-surface thermodynamic gradients [2], atmospheric stability is an important property to consider when evaluating EDs. Ding et al. [39] demonstrated that modeled z_d has a high sensitivity to thermodynamic stability functions used within various models.

Figure 6A illustrates the relationship between c_0 and *Ri* and reveals a nonlinear trend, with c_0 being larger when *Ri* magnitudes are smaller (more negative). Pearson's correlation coefficient between c_0 and *Ri* is -0.87 ($p \sim 0$), indicating a strong, significant inverse relationship, which is visually evident in Figure 6A. It should be cautioned, however, that Pearson's correlation coefficient only quantifies the linear portion of the observed nonlinear relationship. Nonetheless, this linear correlation suggests that as stability decreases (becomes more unstable), c_0 will increase. More broadly, *M*-profiles which have a tighter radius of curvature are likely to be associated with unstable atmospheres. Furthermore, the slope of the relationship between c_0 and *Ri* is steeper when *Ri* is near-neutral ($Ri \sim= 0$) and reduces in steepness when *Ri* indicates large instability ($Ri < -2$). This trend suggests that when *Ri* is near-neutral or stable, the curvature (c_0) of the profile is sensitive to small changes in *Ri*, similar to the findings of Cherrett [24] with respect to stability and the M-deficit. Low scatter is observed near the neutral value for c_0 (i.e., when $Ri = 0$, solid line; $c_0 \approx 0.125$ M-units m^{-1}, dashed line). The larger scatter in this relationship for $Ri < -2$ may be associated with convective conditions.

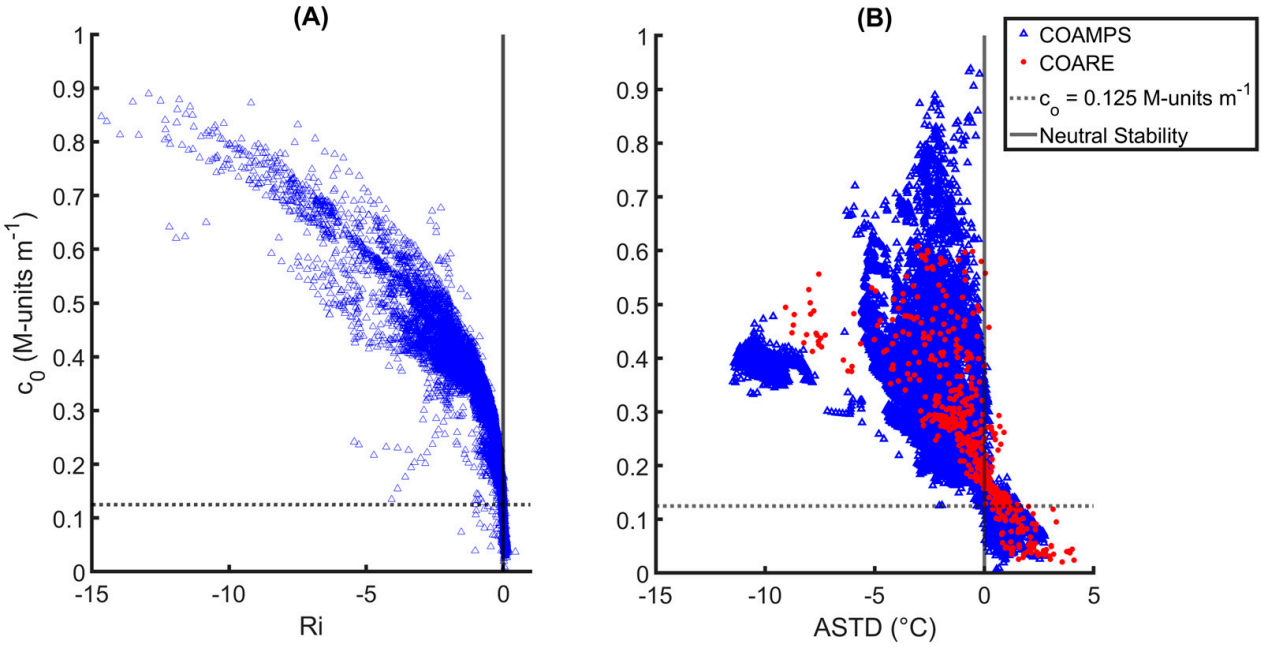


Figure 6. Relationships between stability metrics and c_0. (**A**) shows the relationship between c_0 and *Ri* for COAMPS profiles, while (**B**) shows the relationship between c_0 and ASTD (for all numerical data—see legend).

Like *Ri*, a weak inverse relationship is found between the ASTD and c_0 for both COARE and COAMPS® profiles (Figure 6B); notably, scatter in the data is also reduced near neutral values with a small offset. In stable regimes (i.e., ASTD > 0 °C), c_0 is smaller (mostly less than ~0.2 M-units m^{-1}), indicating broader curvatures, whereas in unstable regimes (i.e., ASTD < 0 °C), c_0 can be large (frequently above ~0.2 M-units m^{-1}), indicating tighter curvature of the M-profiles. There is a subset of COARE and COAMPS® profiles with c_0 between ~0.35 and 0.50 M-units m^{-1} that do not appear to follow the same trends as the data in the near-neutral or mildly unstable regime; they are associated with a very unstable thermal regime (i.e., ASTD < −6 °C). This highly unstable regime, likely at or near convective conditions, could invoke different forms of the stability functions than the more mildly unstable range. Furthermore, the stability functions in this stability range could differ between NAVSLaM and COARE [31] because this regime also exhibits the least overlap in the COARE and COAMPS® predictions. Notably, this subset of points corresponding to COAMPS® profiles (Figure 6B) does not occur as outliers in the relationship between c_0 and *Ri* (Figure 6A), potentially indicating that winds are a factor in the relationship between stability and c_0. It is also noteworthy that when the ASTD > 0, *Ri* is not always greater than zero (and vice versa). This discrepancy occurs due to the conversion of temperatures to virtual temperatures. In some cases, this conversion can change the sign of the temperature gradient. This sign change typically occurs in near-neutral cases or cases with a high water vapor content.

Near-surface wind shear could influence ED properties by mechanical mixing impacting thermodynamic gradients responsible for controlling atmospheric refractivity [29]. For example, McKeon [40] found that RH and temperature weakly influence z_d in times of increased wind speeds. The relationship between c_0 and wind speed shear ($\partial U/\partial z$) is investigated in Figure 7. Notably, c_0 from COARE and COAMPS® behave similarly with respect to $\partial U/\partial z$ (and $\partial q/\partial z$), so they are shown using the same symbols to focus on the overall trends between c_0 and the respective thermodynamic property.

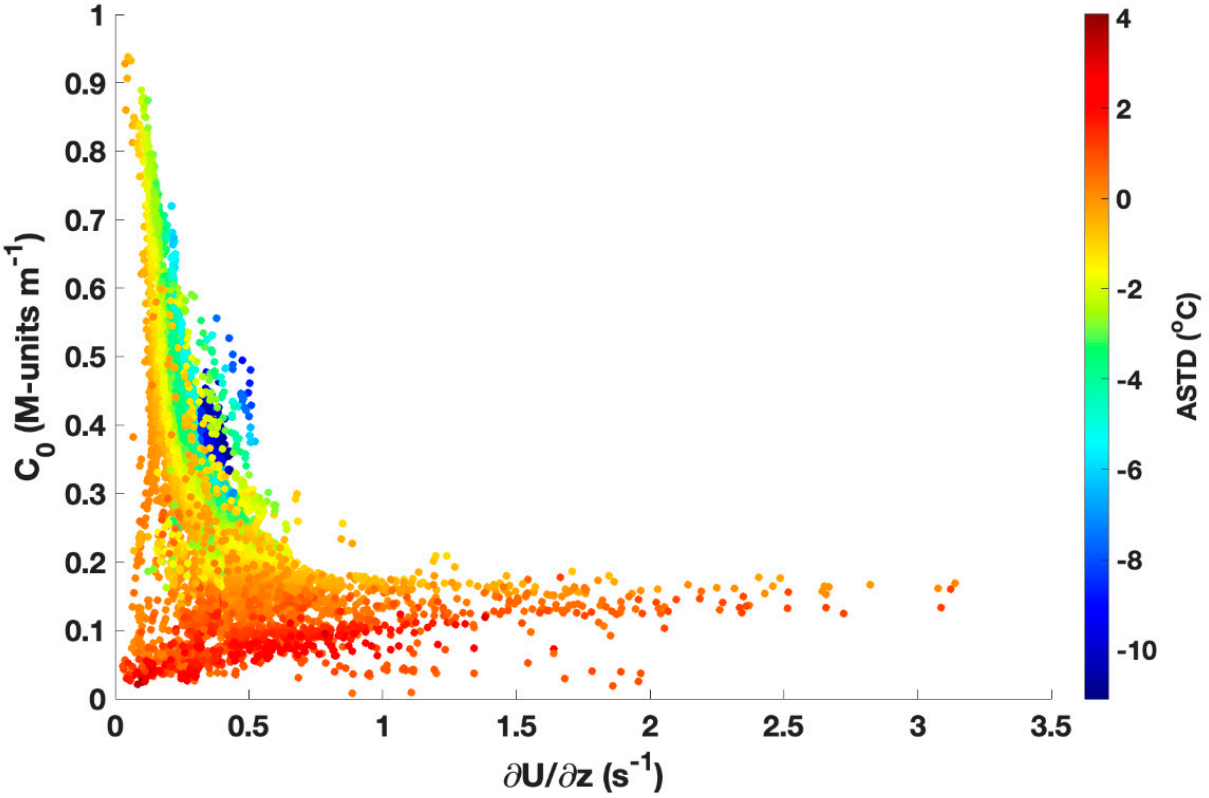


Figure 7. The relationship between c_0 and wind speed shear ($\partial U/\partial z$) for both COARE and COAMPS®. The color of each marker corresponds to the respective ASTD (see color bar).

When wind shear is small (~<1 s^{-1}), the range of c_0 is large (Figure 7), and in contrast, during times of greater wind shear (>1 s^{-1}), c_0 is generally below 0.2 M-units m^{-1}, although it should be noted that limited ASTD conditions were observed under high wind shear. Furthermore, large c_0 (c_0 > 0.5 M-units m^{-1}) only occurs when wind shear is low (< 0.30 s^{-1}) during unstable conditions. These findings could be attributed to limited mechanical mixing allowing for the setup of steeper near-surface thermodynamic gradients during unstable conditions. During conditions that are slightly unstable (i.e., −4 °C < ASTD < 0 °C) and have relatively low wind shear (<1 s^{-1}), c_0 varies significantly with wind shear. However, during neutral to stable conditions, c_0 appears to be relatively insensitive to wind shear, perhaps suggesting that stable stratification limits the influence of wind shear on near-surface thermodynamic gradients and hence evaporation duct shape. During stable conditions (ASTD > 0), the lower c_0 (<0.2 M-units m^{-1}) is consistent with the findings presented in Figure 6 that stable conditions are generally associated with smaller (broader) curvatures (c_0). Notably, Figure 7 shows the very unstable (i.e., ASTD < −6 °C) cluster of points seen in Figure 6B as occurring during a relatively low wind shear of ~0.4 s^{-1} (and c_0 near 0.4 M-units/m).

Lastly, because EDs are purported to form from steep near-surface humidity gradients [2,18], and Pastore et al. [16] suggests that the stability regime and near-surface humidity gradients are likely related to c_0, the relationship between $\partial q/\partial z$ and c_0 is investigated. Specific humidity is used as the humidity metric because it directly measures water content and is not influenced by temperature or pressure. This relationship, also delineated with respect to the ASTD, is illustrated in Figure 8. COARE and COAMPS® c_0 both have a strong inverse linear relationship with $\partial q/\partial z$, implying that $\partial q/\partial z$ is connected to c_0 variations. The coefficients of determination, R^2, for COARE and COAMPS® are both approximately 0.96; thus, 96% of c_0 variance can be explained via a linear relationship with $\partial q/\partial z$. The relationship between $\partial q/\partial z$ and c_0 becomes less consistent when the ASTD

is near-neutral and stable, (ASTD $\gtrsim$ 0 °C) shown by the increased scatter in this region in Figure 8. This result could imply discrepancies between MOST-based models and/or generally more model uncertainty in stable regimes, which is well documented [37,38], or a more limited shape representation by c_0 during stable regimes. The linear relationship appears weakly dependent on the ASTD for neutral and unstable regimes, which is consistent with prior results shown in this manuscript (Figure 6). In strongly unstable regimes (ASTD < −6 °C), as shown previously, the relationship appears to change and become slightly less linear, likely associated with the development of convective conditions. For mildly unstable cases, the relationship indicates that the curvature of the *M*-profile becomes tighter (larger c_0) as the specific humidity gradient becomes more negative (stronger). This high correlation between ∂q/∂z and c_0 suggests that measuring ∂q/∂z may offer enough information to predict the shape of the evaporation duct *a priori*.

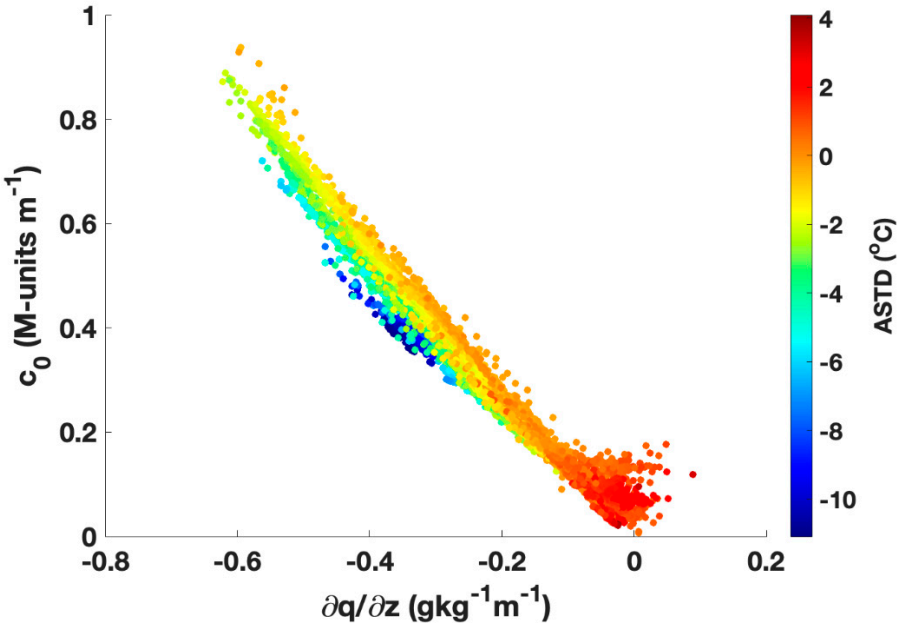


Figure 8. The relationship between the NSSHG ($\partial q/\partial z$) and c_0, where the color of each marker is the respective ASTD for both COARE and COAMPS® (see color bar).

Although the above relationship between c_0 and ∂q/∂z is evident, instrumentation is typically limited in its ability to make accurate measurements of humidity close to the ocean surface due to the fouling of the instrument by sea spray and waves [16,41]; thus, SST and the assumption of 98% relative humidity is more common, as utilized in this study, for the surface-specific humidity. Measuring humidity at altitudes well above the surface can also be challenging due to the need for a weather balloon, rocketsonde, or drone-based measurement. Thus, it becomes important to explore the robustness of the c_0 and ∂q/∂z relationship with respect to both the upper and lower limits of the measurement heights needed to estimate ∂q/∂z for this relationship to remain similar to that demonstrated in Figure 8. This sensitivity analysis is shown in Figure 9. Figure 9A,B show the effect of raising the lower reference altitude on the relationship between ∂q/∂z and c_0. Figure 9C,D show the effect of lowering the upper reference altitude on this relationship. Figure 9E shows where the various reference points are located on an example of a specific humidity profile.

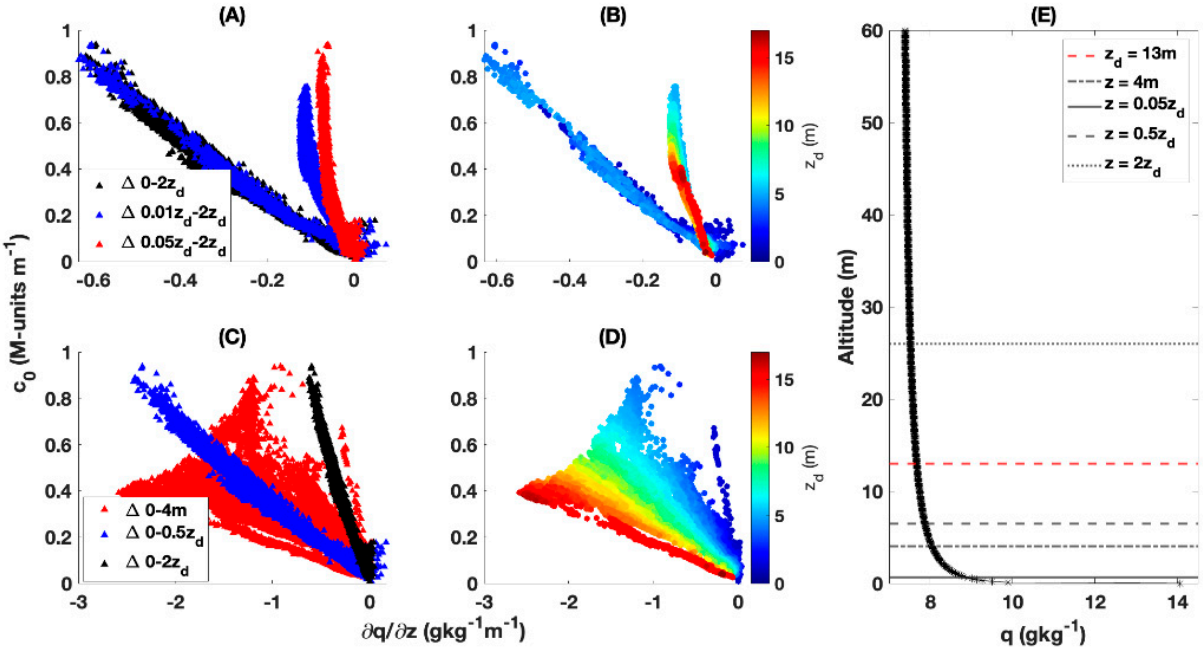


Figure 9. Relationship between c_0 and $\partial q/\partial z$, when $\partial q/\partial z$ is estimated over various altitude ranges. (**A**) shows the relationship between $\partial q/\partial z$ and c_0 when the lower reference altitude is varied (see legend). (**B**) shows the relationship between $\partial q/\partial z$ and c_0 when $\partial q/\partial z$ is computed using the altitude range of $0.01z_d$–$2z_d$ and where the color of each marker is the respective z_d (see color bar). (**C**) shows the relationship between c_0 and $\partial q/\partial z$ when the upper reference altitude is varied (see legend). (**D**) shows the relationship between $\partial q/\partial z$ and c_0 when $\partial q/\partial z$ is computed using the altitude range of 0 m–4 m and where the color of each marker is the respective z_d (see color bar). (**E**) Example COAMPS® vertical q profile from 30 October 2015, at 1300Z, where the corresponding M-profile z_d is 13 m (red dashed line) and the height of various reference points on the profile are illustrated (see legend).

The relationship between c_0 and $\partial q/\partial z$, as shown in Figure 8, is also shown in Figure 9A,C as the black markers. However, it can be easily observed in Figure 9A that when the lower reference altitude for $\partial q/\partial z$ changes to 1% of z_d (blue markers), the relationship bifurcates (or splits) into two different relationships, where some profiles show the same relationship as when the lower reference altitude is at $z = 0$ m (black markers) and another branch shows a different relationship. If this lower reference is raised even higher to 5% of the duct height (Figure 9A red markers), then the relationship observed when the lower reference altitude is at $z = 0$ m no longer exists for any profile. Examining the bifurcated case more closely, shown in Figure 9B, one branch of the bifurcated case (the one consistent with trends in Figure 8) is composed of profiles with lower duct heights, while the other branch is composed of profiles with higher duct heights. This result suggests that there is a somewhat fixed limit to how high the lower reference altitude for estimating $\partial q/\partial z$ can be for the relationship shown in Figure 8 to hold. Higher duct heights mean that 1% of the duct height is also a larger number; thus, in those cases, the lower reference altitude is higher than in cases with a smaller duct height, explaining the bifurcation by duct height shown in Figure 9B. More specifically, 1% of z_d in profiles that continue to follow the trends shown in Figure 8 correspond to heights of less than 10 cm above the surface. This result suggests that the very-near-surface region ($\lesssim$10 cm) is critical for the prediction of the duct shape parameter (c_0) using only an estimated $\partial q/\partial z$. Additionally, this result indicates that c_0 estimation requires an SST estimate (and assumption of 98% relative humidity) because making a humidity measurement this close to the surface is logistically challenging. The collapse of the relationship when the lower reference altitude is higher (e.g., 5% of z_d) indicates that the steepest portion of the humidity profile occurs

before this height (see Figure 9E); this height limit could be related to a physical aspect of the boundary layer such as the bottom/start of the constant flux layer. Thus, to be able to utilize the linear relationship between $\partial q/\partial z$ and c_0 in a predictive manner, as presented here, the two measurements used to compute $\partial q/\partial z$ need to be obtained such that the lower measurement is taken at the surface.

In contrast, Figure 9C shows that when the upper reference altitude is set to a fixed value, such as 4 m, typical of a buoy-based measurement for example (see Figure 9E), the relationship in Figure 8 no longer collapses on a single linear slope but instead shows variability in slope (relative to Figure 8). Figure 9D shows that this variability is duct-height-dependent, suggesting that the humidity gradient impacting c_0 is not being consistently captured across profiles to result in a consistent relationship. In fact, the predictive relationship only holds in cases where the upper reference altitude for $\partial q/\partial z$ is calculated with respect to the duct height, shown in Figure 9C (blue and black markers). When the upper reference altitude for computing $\partial q/\partial z$ is $0.5z_d$ or $2z_d$ (see Figure 9E), the coefficients of determination (R^2) are 0.97, whereas the R^2 when using an upper reference altitude of $0.25z_d$ is lower (0.93), indicating that the entire humidity gradient impacting c_0 (or the M-deficit) is no longer being captured. Therefore, we suggest that the upper reference altitude be at least half the duct height; however, it should be noted that the linear relationship using an upper reference altitude of $0.5z_d$ is different than that for $2z_d$ (even though they both collapse the data; Figure 9C).

4. Conclusions

Two numerical datasets based on two different numerical modeling approaches—COAREand COAMPS®—estimated and verified against *in situ* data for the CASPER east field campaign were utilized to analyze relationships between a model parameter describing ED shape, c_0, and atmospheric properties: ASTD, Ri, $\partial q/\partial z$, and wind shear. The gradient Richardson number and ASTD are shown to be inversely correlated to c_0, suggesting that as the atmosphere becomes more unstable, the shape of the duct (i.e., the duct curvature) will become tighter, or more "curved" for a given duct height. Inversely, during stable conditions, lower c_0 should be expected, leading to broader-curved M-profiles. When wind shear is low (<0.5 s^{-1}), and the ASTD is negative, c_0 varies considerably with wind shear, but when the ASTD is positive, wind shear has little impact on duct shape (c_0) for the range of the stabilities examined here.

Finally, c_0 is shown to have the strongest inverse correlation with $\partial q/\partial z$, suggesting that ED shape is most sensitive to the humidity gradients below the duct height. This relationship was shown to be slightly ASTD-dependent and indicates increasingly tighter M-profile curvatures as the specific humidity gradient strengthens (becomes more negative). The robust relationship suggests that the NSSHG may be used to predict c_0 or ED shape *a priori* with few supporting measurements and an estimated duct height, where the latter could be obtained through inversion methods [18–20]. Further evaluation of the relationship between c_0 and $\partial q/\partial z$ suggests that the two measurements of specific humidity should minimally span from the surface to at least $0.5z_d$ (see Figure 9E) to obtain predictive capabilities with c_0. In other words, ED shape (i.e., trapping strength) for X-band EM propagation can be reasonably estimated with an SST measurement (assuming 98% relative humidity) and one measurement of specific humidity at a higher altitude (>$0.5z_d$), which are relatively simple and straightforward measurements to make. With the ED shape parameter estimated, propagation predictions based on simple parametric refractivity models will be more accurate as the duct strength will be accounted for more accurately than using, for example, the commonly assumed neutral value of 0.125 M-units m^{-1}. This approximation (in conjunction with estimating duct height) would significantly reduce the required data and subsequent computation time to estimate the refractive environment. For example, the use of MOST requires a wind speed measurement in addition to temperature and humidity measurements at a reference height and at the surface. Further, parametric propagation studies using a parametric refractivity model can more easily and accurately

explore a wide range of conditions by varying the duct shape (c_0), with small c_0 during stable conditions and large c_0 during unstable conditions (for a given duct height).

It should be noted that the results of this study are based on numerical datasets from a single field campaign on the east coast of the United States during autumn. In this field campaign, warmer sea surface temperatures frequently led to unstable atmospheres and higher rates of evaporation than may be valid for other parts of the globe. In addition, all the datasets used in this study rely on MOST to some extent and are subject to the limitations of this theory. Further research should investigate whether these results hold true across a wider range of conditions, particularly those with cooler sea surface temperatures. Limited profiles for the stable regime exist in this dataset, so more research on these relationships during stable atmospheric conditions is needed. Importantly, this work should be verified with measured *in situ* data and highlights the importance of measuring humidity near the ocean surface. Improvements in technologies that can reliably make these near-surface humidity measurements are needed.

Collectively, this manuscript demonstrates how evaporation duct shape can vary independently from duct height and that these variations can be linked to atmospheric conditions, especially the humidity gradients near the surface. Furthermore, these results increase the relevance and applicability of simple log-linear *M*-profile models (e.g., Equation (1)) to estimate refractive environments for the design, development, testing, and operation of X-band radar-based technologies used in a wide range of applications involving communications, detection, and forecasting.

Author Contributions: Conceptualization, E.E.H.; methodology, D.P.G., E.E.H. and S.E.W.; formal analysis, D.P.G. and S.E.W.; investigation, D.P.G., E.E.H. and S.E.W.; data curation, T.H. and S.E.W.; writing—original draft preparation, S.E.W.; writing—review and editing, D.P.G., T.H., E.E.H. and S.E.W.; visualization, D.P.G. and S.E.W.; supervision, E.E.H.; project administration, E.E.H.; funding acquisition, E.E.H. All authors have read and agreed to the published version of the manuscript.

Funding: This research was partly supported by the Office of Naval Research (grant N00014-19-1-2350) and Coastal Carolina University internal student fellowships.

Institutional Review Board Statement: Not applicable.

Informed Consent Statement: Not applicable.

Data Availability Statement: The original contributions presented in the study are included in the article, further inquiries can be directed to the corresponding author/s.

Acknowledgments: The authors would like to thank Qing Wang from the Naval Postgraduate School, Tony de Paolo and Eric Terrill at the Coastal Observing Research and Development Center at the Scripps Institute of Oceanography, and the entire CASPER project team for providing the meteorological and wave buoy data used in this study.

Conflicts of Interest: The authors declare no conflicts of interest.

References

1. Babin, S.M.; Young, G.S.; Carton, J.A. A new model of the oceanic evaporation duct. *J. Appl. Meteorol.* **1997**, *36*, 193–204. [CrossRef]
2. Skolnik, M.I. *Introduction to Radar Systems*, 3rd ed.; McGraw-Hill: New York, NY, USA, 2003.
3. Gunashekar, S.D.; Warrington, E.M.; Siddle, D.R. Long-term statistics related to evaporation duct propagation of 2 GHz radio waves in the English Channel. *Radio Sci.* **2010**, *45*, RS6010. [CrossRef]
4. Grimes, N.G.; Hackett, E.E. Examining constants in the Paulus-Jeske evaporation duct model. In Proceedings of the United States National Committee of URSI National Radio Science Meeting, Boulder, CO, USA, 8–11 January 2014.
5. Mufti, N.; Siddle, D.R. Investigations into the occurrence of evaporation ducts within the English channel. In Proceedings of the IEEE-APS Topical Conference on Antennas and Propagation in Wireless Communications, Cairns, Australia, 19 September 2016.
6. Ulate, M.; Wang, Q.; Haack, T.; Holt, T.; Alappattu, D.P. Mean offshore refractive conditions during the CASPER east field campaign. *J. Appl. Meteorol. Climatol.* **2019**, *58*, 853–874. [CrossRef]
7. Fairall, C.W.; Bradley, E.F.; Hare, J.E.; Grachev, A.A.; Edson, J.B. Bulk parameterization of air-sea fluxes: Updates and verification for the COARE algorithm. *J. Clim.* **2003**, *16*, 571–591. [CrossRef]
8. Penton, S.E.; Hackett, E.E. Rough Ocean surface effects on evaporative duct atmospheric refractivity inversions using genetic algorithms. *Radio Sci.* **2018**, *53*, 804–819. [CrossRef]

9. Paulus, R.A. Evaporation duct effects on sea clutter. *IEEE Trans. Antenn. Propag.* **1990**, *38*, 1765–1771. [CrossRef]
10. Saeger, J.T.; Grimes, N.G.; Rickard, H.E.; Hackett, E.E. Evaluation of simplified evaporation duct refractivity models for inversion problems. *Radio Sci.* **2015**, *50*, 1110–1130. [CrossRef]
11. Wu, J. Wind-Stress coefficients over Sea surface near Neutral Conditions—A Revisit. *J. Phys. Oceanogr.* **1980**, *10*, 727–740. [CrossRef]
12. Zhang, J.-P.; Wu, X.-S.; Zhu, Q.-L.; Wang, B. A four-parameter M profile model for the evaporation duct estimation from radar clutter. *Prog. Electromagn. Res.* **2011**, *114*, 353–368. [CrossRef]
13. Rogers, L.; Hattan, C.; Stapleton, J. Estimating evaporation duct heights from radar sea echo. *Radio Sci.* **2000**, *35*, 955–966. [CrossRef]
14. Gerstoft, P.; Rogers, L.T.; Krolik, J.L.; Hodgkiss, W.S. Inversion for refractivity parameters from radar sea clutter. *Radio Sci.* **2003**, *38*, 8053. [CrossRef]
15. Wang, Q.; Burkholder, R.J.; Yardim, C.; Xu, L.; Pozderac, J.; Christman, A.; Fernando, H.J.; Alappattu, D.P.; Wang, Q. Range and Height Measurement of X-Band EM Propagation in the Marine Atmospheric Boundary Layer. *IEEE Trans. Antennas Propag.* **2019**, *67*, 2063–2073. [CrossRef]
16. Pastore, D.M.; Greenway, D.P.; Stanek, M.J.; Wessinger, S.E.; Haack, T.; Wang, Q.; Hackett, E.E. Comparison of atmospheric refractivity estimation methods and their influence on radar propagation predictions. *Radio Sci.* **2021**, *56*, 1–17. [CrossRef]
17. Lentini, N.E.; Hackett, E.E. Global sensitivity of parabolic equation radar wave propagation simulation to sea state and atmospheric refractivity structure. *Radio Sci.* **2015**, *50*, 1027–1049. [CrossRef]
18. Karimian, A.; Yardim, C.; Haack, T.; Gerstoft, P.; Hodgkiss, W.S.; Rogers, T. Toward the assimilation of the atmospheric surface layer using numerical weather prediction and radar clutter observations. *J. Appl. Meteorol. Clim.* **2013**, *52*, 2345–2355. [CrossRef]
19. Pozderac, J.; Johnson, J.; Yardim, C.; Merrill, C.; de Paolo, T.; Terrill, E.; Ryan, F.; Frederickson, P. X-Band Beacon-Receiver Array Evaporation Duct Height Estimation. *IEEE Trans. Antenn. Propag.* **2018**, *66*, 2545–2556. [CrossRef]
20. Pastore, D.M.; Wessinger, S.E.; Greenway, D.P.; Stanek, M.J.; Burkholder, R.J.; Haack, T.; Wang, Q.; Hackett, E.E. Refractivity inversions from point-to-point X-band radar propagation measurements. *Radio Sci.* **2022**, *57*, 1–16. [CrossRef]
21. Pekeris, C. Wave theoretical interpretation of propagation of 10-centimeter and 3-centimeter waves in low level ocean ducts. *Radio Sci.* **1947**, *35*, 453–467. [CrossRef]
22. Katzin, M.; Bauchman, R.W.; Binnian, W. 3- and 9-centimeter propagation in low ocean ducts. *Proc. IRE* **1947**, *35*, 891–905. [CrossRef]
23. Hitney, H.V.; Veith, R. Statistical assessment of evaporation duct propagation. *IEEE Trans. Antenn. Propag.* **1990**, *38*, 794–799. [CrossRef]
24. Cherrett, R.C. Capturing Characteristics of Atmospheric Refractivity Using Observations and Modeling Approaches. Ph.D. Thesis, Naval Postgraduate School, Monterey, CA, USA, 2015.
25. Zhang, Q.; Yang, K.; Yang, Q. Statistical analysis of the quantified relationship between evaporation duct and oceanic evaporation for unstable conditions. *J. Atmos. Ocean. Technol.* **2017**, *34*, 2489–2497. [CrossRef]
26. Wang, Q.; Alappattu, D.P.; Billingsley, S.; Blomquist, B.; Burkholder, R.J.; Christman, A.J.; Creegan, E.D.; de Paolo, T.; Eleuterio, D.P.; Fernando, H.J.; et al. CASPER: Coupled air–sea processes and electromagnetic ducting research. *Bull. Amer. Meteor. Soc.* **2018**, *99*, 1449–1471. [CrossRef]
27. Fairall, C.W.; Bradley, E.F.; Rogers, D.P.; Edson, J.B.; Young, G.S. Bulk parameterization of air-sea fluxes for tropical ocean-global atmosphere coupled-ocean 91 atmosphere response experiment. *J. Geophys. Res. Oceans* **1996**, *101*, 3747–3764. [CrossRef]
28. Plant, W.J. The ocean wave height variance spectrum: Wavenumber peak versus frequency peak. *J. Phys. Oceanogr.* **2009**, *39*, 2382–2383. [CrossRef]
29. Bean, B.R.; Dutton, E.J. *Radio Meteorology*, 1st ed.; College Entrance Book Company: New York, NY, USA, 1968.
30. Hodur, R.M. The Naval Research Laboratory's Coupled Ocean/Atmosphere Mesoscale Prediction System (COAMPS®). *Mon. Weather Rev.* **1997**, *125*, 1414–1430. [CrossRef]
31. Frederickson, P.A. Further improvements and validation for the Navy Atmospheric Vertical Surface Layer Model (NAVSLaM). In Proceedings of the 2015 USNC-URSI Radio Science Meeting (Joint with AP-S Symposium), Vancouver, BC, Canada,, 19–24 July 2015; p. 242. [CrossRef]
32. Hogan, T.F.; Rosmond, T.E. The description of the Navy Operational Global Atmospheric Prediction System's spectral forecast model. *Mon. Weather Rev.* **1991**, *119*, 1786–1815. [CrossRef]
33. Halliwell, G.R.; Bleck, R.; Chassignet, E.P. Atlantic Ocean simulations performed using a new hybrid-coordinate ocean model. In Proceedings of the Fall 1998 AGU Meeting, San Francisco, CA, USA, 6–10 December 1998.
34. Matsko, I.J.; Hackett, E.E. Impact of radar data sampling on the accuracy of atmospheric refractivity inversions over marine surface. *Radio Sci.* **2019**, *54*, 704–714. [CrossRef]
35. Gossard, E.E.; Strauch, R.G. *Radar Observation of Clear Air and Clouds*; Elsevier: New York, NY, USA, 1983.
36. Businger, J.A.; Wyngaard, J.C.; Izumi, Y.; Bradley, E.F. Flux profile relationships in the atmospheric surface layer. *J. Atmos. Sci.* **1971**, *28*, 181–189. [CrossRef]
37. Panofsky, H.A.; Dutton, J.A. *Atmospheric Turbulence: Models and Methods for Engineering Applications*; John Wiley & Sons: New York, NY, USA, 1984.

38. Mauristen, T.; Svensson, G.; Zilitinkevich, S.S.; Esau, I.; Enger, L.; Grisogono, B. A total turbulent energy closure model for neutrally and stably stratified atmospheric boundary layers. *J. Atmos. Sci.* **2007**, *64*, 4113–4126.
39. Ding, J.; Fei, J.; Huang, X.; Cheng, X.; Hu, X.; Ji, L. Development and validation of an evaporation duct model. Part I: Model establishment and sensitivity experiments. *J. Meteorol. Res.* **2015**, *29*, 467–481. [CrossRef]
40. McKeon, B.D. Climate Analysis of Evaporation Ducts in the South China Sea. Master's Thesis, Naval Postgraduate School, Monterey, CA, USA, 2013.
41. Kang, D.; Wang, Q. Optimized estimation of surface layer characteristics from profiling measurements. *Atmosphere* **2016**, *7*, 14. [CrossRef]

Disclaimer/Publisher's Note: The statements, opinions and data contained in all publications are solely those of the individual author(s) and contributor(s) and not of MDPI and/or the editor(s). MDPI and/or the editor(s) disclaim responsibility for any injury to people or property resulting from any ideas, methods, instructions or products referred to in the content.